Costa, C.; Reizabal, A.; Sabater I Serra, R.; Andrio Balado, A.; Pérez-Álvarez, L.; Gómez Ribelles, JL.; Vilas-Vilela, J.... (2021). Broadband dielectric response of silk Fibroin/BaTiO3 composites: Influence
of nanoparticle size and concentration. Composites Science and Technology. 213:1-10. https://doi.org/10.1016/j.compscitech.2021.108927

Broadband Dielectric Response of Silk Fibroin/$BaTiO_3$ Composites: Influence of Nanoparticle Size and Concentration

C.M. Costa[1,2#*], A. Reizabal[3,4#], R. Sabater i Serra[5,6], A. Andrio Balado[7], L. Pérez-Álvarez[3,4], J. L. Gómez Ribelles[5,6], J.L. Vilas-Vilela[3,4], S. Lanceros-Méndez[3,8*]

[1]Centro de Física, Universidade do Minho, 4710-057 Braga, Portugal

[2]Institute of Science and Innovation for Bio-Sustainability (IB-S), University of Minho, 4710-053 Braga, Portugal

[3]BCMaterials, Basque Center for Materials, Applications and Nanostructures, UPV/EHU Science Park, 48940 Leioa, Spain

[4]Departamento de Química Física, Facultad de Ciencia y Tecnología, Universidad del País Vasco/EHU, Apdo. 644, Bilbao, Spain

[5]Centre for Biomaterials and Tissue Engineering, CBIT, Universitat Politècnica de València, 46022, Valencia, Spain

[6]Biomedical Research Networking Center on Bioengineering, Biomaterials and Nanomedicine (CIBER-BBN), Valencia, Spain

[7]Departament de Física, Universitat Jaume I, 12071 Castellón, Spain

[8]Ikerbasque, Basque Foundation for Science, 48009 Bilbao, Spain

[#]equal contribution

Keywords: A. Nano particles; A. Nano composites; A. Polymer matrix composites (PMCs); A. Smart materials

[*] **Corresponding Authors**

C.M. Costa (cmscosta@fisica.uminho.pt), S. Lanceros-Méndez (senentxu.lanceros@bcmaterials.net)

Abstract: In order to advance towards more sustainable electronics generation, natural polymers with tailored dielectric response are essential. In this search, the combination of bio-based materials with active fillers in composite form, suppose one of the most viable alternatives. To achieve it, this work has explored the ability to control dielectric response of Silk Fibroin, a protein polymer by its combination with ceramic barium titanate ($BaTiO_3$) nanoparticles. Both the effect of filler concentration (0, 5, 10, 20 and 40 wt.%) and size (100 and 200 nm) has been studied in composites processed by easily scalable techniques. Samples with a homogeneous distribution of nanoparticles have been obtained. Dielectric relaxation processes assessed by broadband dielectric relaxation spectroscopy (BDS) in wide frequency (0.1 Hz–1 MHz) and temperature ranges (- 40 to 220 ºC), revealed a dielectric constant increasing with filler content and decreasing with filler size, ranging from 4.4 for SF up to 142 for the SF/$BaTiO_3$ composite with 40 wt. %, at room temperature and 1 kHz. Two relaxations processes are observed, the β-relaxation and the conductivity relaxation, both with temperature-dependent behaviour. The activation energy of the conductivity process decreases with increasing nanoparticle content and decreasing size. A Maxwell-Wagner-Sillar process related to the interface between the silk fibroin matrix and the $BaTiO_3$ nanoparticles was also identified.

1. Introduction

Non-renewable resources over extraction, industrial intensive production and mismanagements of consumer waste have led to serious global environmental damage [1, 2]. Among the strategies proposed to achieve a harmonious relationship between humans and environment, an alternative approach is proposed based on the promotion of a more responsible exploitation and use of resources while current lifestyle is preserved [3]. This essentially ecological economy follows the principles of: i) reducing the use of resources, ii) reusing the materials produced and iii) recycling waste to incorporate it again in other

facilities or uses [4]. However, in order to achieve a real circular economy in which products are extracted directly from nature and returned to it without major ecological impacts, it is necessary to address the origin of the resources. Bio-based materials, obtained from renewable natural resources have been listed as a promising approach for this purpose [5]. Its advantages consist mainly of its i) natural origin, ii) abundance in nature and iii) capability to be naturally degraded, which facilitates the sustainability of derived materials production, guarantees the availability of resources and reduces the environmental impacts of waste disposal. Therefore, the circular economy focuses on replacing synthetic polluting materials by bio-based materials. For that, it is necessary to design a new generation of bio-based materials capable of responding to strict and specific technological demands, combining the advantages of their predecessors [6, 7].

Among bio-based materials, silk fibroin (SF), a semi-crystalline fibre-like protein obtained from silkworm cocoons, represents an interesting choice for its unique properties, easy processing and tunnability [8]. As a protein, SF is formed by repetitive sequences of amino acids ordered in large polypeptide chains. Its composition consists mainly on Gly (~ 45%), Ala (~ 29%), Ser (~ 12%) and Gly (~ 5%) amino acids [9], structured into repetitive sequences (Gly-Ala-Gly-Ala-Gly-(Ser/Gly)) forming highly packed crystalline domains and non-repetitive sequences giving place to amorphous domains [9-11]. The presence and combination of both crystalline and amorphous domains with SF macroscopic configuration will mainly define the properties of SF-derived materials [8]. Control of crystalline and amorphous domains, therefore, will provide a useful tool for programming the SF-based macroscopic properties and therefore will define their performance of SF based materials when are incorporated into devices [8].

From the point of view of materials science, natural SF is characterized by a high mechanical strength (up to 690 MPa) [12], flexibility, thermal stability above 300 ºC [13], high dielectric constant ($\varepsilon' = 5$) [14] and biocompatibility [15]. SF can be easily dissolved in water, maintaining its stability and can be processed into a variety of formats such as films, porous structures, micro- and nanoparticles and gels, among others which can easily become water stable [8, 16]. In addition, the versatile polypeptide composition endows SF with several active groups that facilitate its functionalization [17] and enable its combination with complementary components to form composite materials [14]. In this way, SF has been successfully combined with polymers and bio-materials to tune properties like biodegradability [18, 19], mechanical properties [20] and biological response [21], with conductive fillers to improve electrical conductivity [14, 22], with active particles for environmental remediation [23, 24] and with cells [15] or drugs [25] for biomedical applications.

Among the possible application fields, SF has attracted great interest in electronics and energy harvesting [26], where it has been applied both as a passive or active material [27]. As a passive material, SF has been used in films manufacturing, due to its self-standing capacity, smooth surface [28], high transparency (> 90% in the visible region) [29], large refractive index [30] and waveguiding properties (~ 2.8 $dB \cdot mm^{-1}$) [31]. In this way, neat SF films have been applied as flexible electronics substrate [27], dielectric gate [32] and in optoelectronics [31]. In addition, due to SF facility to be combined with other materials, SF composites have been used as active materials in organic field-effect transistors (EFETs) [32], resistive-switching devices [33], nanogenerators [34, 35] and for energy harvesting [36]. The growing interest in this field makes clear the need for a deep understanding of the main dielectric properties of SF, as well as on the possible ways to tune them.

In this context, this study has focused on revealing the SF dielectric response in a broad range of temperature and frequency. In addition, SF was combined with large dielectric constant ceramic nanoparticles to enhance its inherent properties. For this purpose, barium titanate ($BaTiO_3$), a ferroelectric material of the perovskite family, was selected due to its high dielectric behaviour, non-polluting nature, simple and cheap preparation, compatibility with organic biological systems and large use in electronic and energy industry [37, 38]. Thus, the effect of $BaTiO_3$ nanoparticles size and concentration on the dielectric properties of SF was studied.

The processing of the new multifunctional composites, considering the principles of minimization of resources with a focus on sustainability, was carried out through techniques with reduced complexity, materials and energy minimization and reduced pollution in order to facilitate the implementation of SF for a next generation of bio-based electronic materials.

2. Materials and methods

2.1. Materials

Bombyx mori silkworm cocoons were supplied by APPACDM, Castelo Branco (Portugal). Formic acid, Sodium Carbonate (Na_2CO_3) and Calcium Chloride ($CaCl_2$), were purchased from Sigma-Aldrich. Spherical nanoparticles of barium titanate ($BaTiO_3$) with two different grain sizes (100 nm and 200 nm), 99.9% purity and a density of 5.85 $g.cm^{-3}$ were provided by SkySpring Nanomaterials.

2.2. Nanocomposites preparation

Composites processing was divided in two stages as is described in the Figure S1. Firstly, the bio-based Silk fibroin (SF) was extracted and processed. In a second stage the SF was combined with $BaTiO_3$ fillers, previously sonicated for 2 hours in the solvent to reduce

agglomeration, to achieve active nanocomposites. Detailed information on composite preparation is presented as supplementary information S1.

2.3. Characterization techniques

The morphology of the samples was evaluated by scanning electron microscopy (SEM) with a NanoSEM - FEI Nova 200 (FEG/SEM). Fourier Transform infrared (FTIR) spectroscopy in the Attenuated Total Reflectance (ATR) mode (Jasco FT/IR-4100) was used to evaluate the influence of the fillers on the SF matrix as well as the molecular insight of the composites. Differential scanning calorimetry (Mettler Toledo DSC 822e equipment) allowed to determine the thermal behaviour of the samples and dielectric measurements were carried out with an impedance analyzer Alpha-S. The isothermal experiments were performed from −40 to 140 °C (thermal stability: 0.5 °C) in 5 °C steps in a frequency range from 0.1 Hz to 1 MHz. Further experimental details are shown as supplementary information S2.

3. Results and discussion

3.1. Morphological analysis and molecular organization

As can be observed in optical photography's (Figure 1a), the processed SF/$BaTiO_3$ nanocomposites behave as self-standing films even at thickness of below 50 μm. All of them show macroscopically and despite of their filler concentration and size, smooth surfaces with homogenous fillers distribution, cream coloration and large transparency.

To evaluate the morphology of SF/$BaTiO_3$ composites, the dispersion and distribution of the fillers and fillers-matrix interphase contacts, SEM images were used. The studied surface and cross sections images are shown in Figure 1b. SF film and SF/ $BaTiO_3$ nanocomposites with 10 wt. % and 40 wt. % were selected as representative for all nanocomposites. The SEM images of the other nanocomposites are shown in Figure S2.

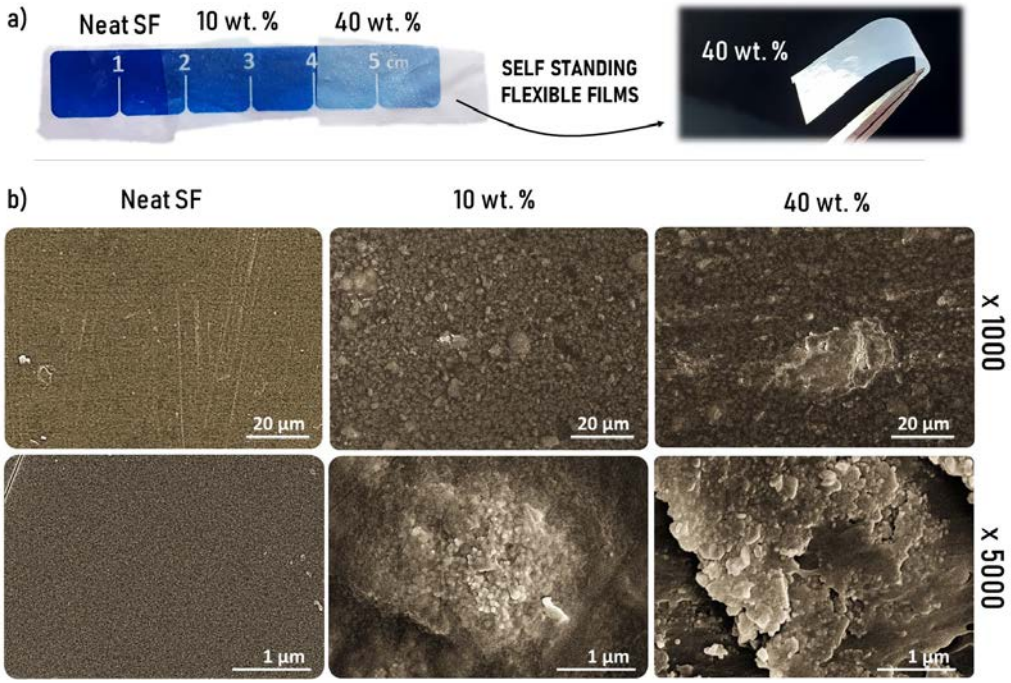

Figure 1 - a) Optical images of SF and SF/$BaTiO_3$ nanocomposites with variable fillers addition and b) SEM images of neat SF films, SF/$BaTiO_3$ 10 wt. % and 40 wt.% composites at different magnifications.

As can be observed in the SEM low magnification images (x1000), the smooth and compact structure of SF is preserved in nanocomposites, regardless of the fillers amount. This behaviour is shown in Figure S2 for the other SF/$BaTiO_3$ nanocomposites. This suggesting that nanoparticles addition has low influence in the SF casting process and samples formation.

The higher magnification SEM images (x5k), show a certain nanoparticles agglomeration on the surface, leading to island-like structures of few microns. These concentrated areas increase in size until 40 wt. % concentration, in which almost continuous phase of nanoparticles is formed. Despite these concentrated areas, the homogeneity is preserved in all the samples, either in particles or clusters distribution.

The influence of $BaTiO_3$ nanoparticle addition on SF molecular structure was evaluated by FTIR, showing that filler concentration and size does not affect the vibrational bands

of the secondary structures of SF (Figure S3a-c). Further information and discussion are shown as supplementary information S3.

Similarly, differential calorimetry results show that SF/$BaTiO_3$ nanocomposites preserve the overall thermal behaviour of SF (Figure S3d). Further information and discussion are shown as supplementary information S3.

SF is stable in water since during the sample processing, the cross-linked configuration is formed. This process is further improved by formic acid casting, since the solvent is able to remove the water molecules trapped inside the SF molecules, promoting the molecular interactions and β-sheets formation. The process could be hindered due to fillers interactions with SF, however, as observed in Figure S3c, the SF/$BaTiO_3$ composites show β-sheets contents above 40%. This shows that $BaTiO_3$ does not hinder crystalline units formation, the processed films remaining highly stable in water [8].

3.2. Dielectric and electric modulus formalism

Dielectric analysis was carried out as a function of frequency (0.1 Hz–1 MHz) and temperature (- 40 to 220 ºC) in order to assess the dynamic dielectric response of neat SF and SF/$BaTiO_3$ nanocomposites related to electric charge carriers and conformational mobility [39]. Real (ε') and imaginary (ε'') parts of the dielectric permittivity in function of frequency and temperature are found in Figures 2a-c) and 2b-d**,** respectively, for neat SF and 40 wt. % SF/ $BaTiO_3$. As representative for all the samples neat SF and 40 wt.% SF/$BaTiO_3$ have been only plotted.

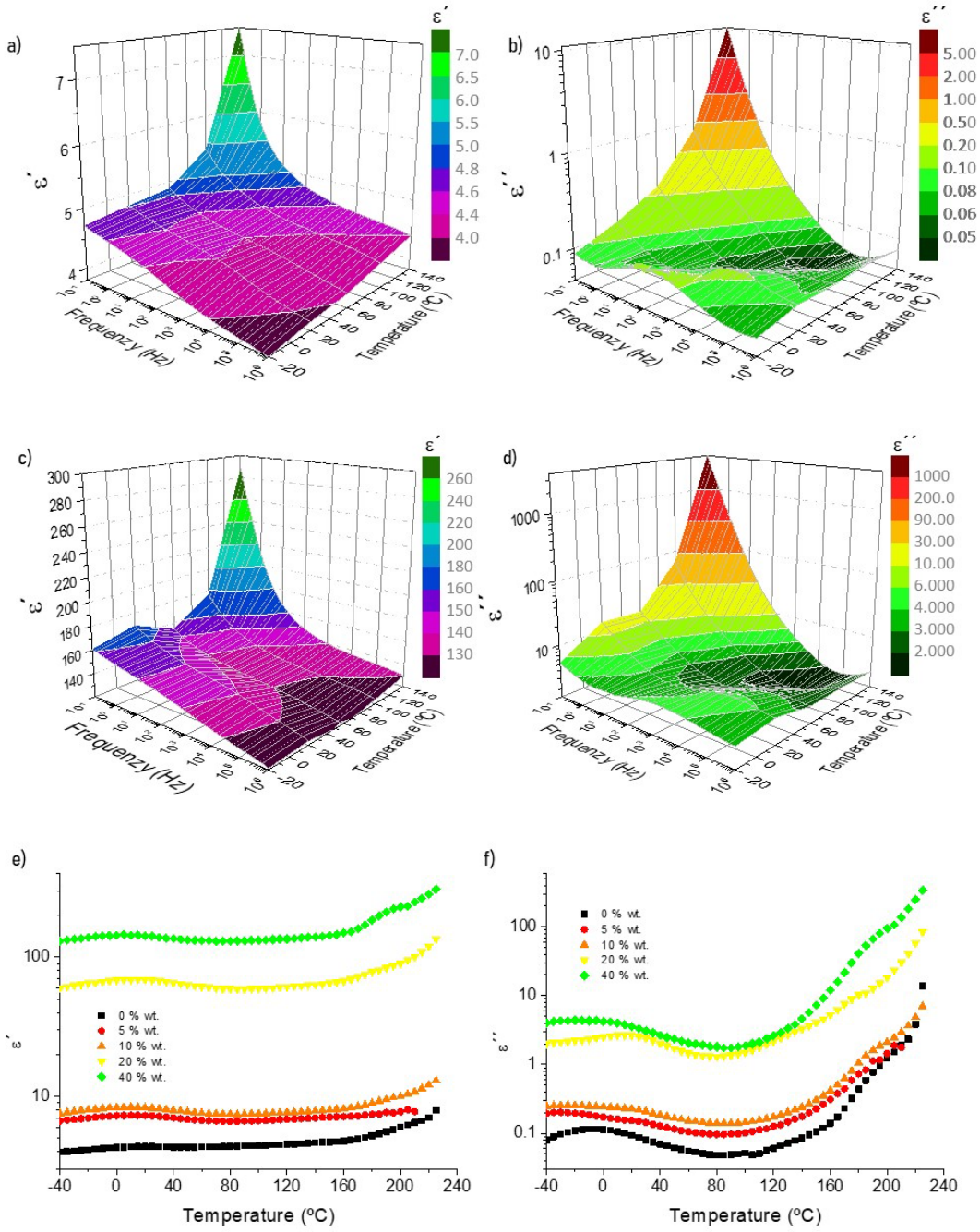

Figure 2 - Temperature and frequency dependence curves of real (ε') and imaginary (ε'') parts of the permittivity of a-c) neat SF and b-d) 40 wt.% SF/$BaTiO_3$, respectively. e) ε' and f) ε'' Isochronal curves as a function of temperature at 10^3 Hz for SF/$BaTiO_3$ composites up to 40 wt.%.

As can be observed, the ε' of neat SF is between 4 -7 in all the frequency range and regardless the temperature (Figure 2a). These values are common for proteins with few

polarizable units and are agree with previously reported data [29, 40]. $BaTiO_3$ nanoparticles addition, induce substantial rise of this value. This can be observed in Figure 2b for single 40wt. % SF/$BaTiO_3$ (in function of temperature and frequency) and in Figure 2e for all the samples (in function of temperature). This significant increase can be mainly attributed to the large polarizability of $BaTiO_3$ nanoparticles (ε'=1260–1700). This mainly because the positively charged titanium ions (Ti_4^+) composing the $BaTiO_3$ crystalline structure, are easily oriented towards the negative pole under an applied electrical field effect [41, 42]. For all the samples the ε' increasing follows a tendency with fillers addition, but it is to mention the sharp ε′ increasing behaved between 10wt. % SF/ $BaTiO_3$ (8 at 20ºC and 10^3 Hz respectively) and 20-40wt. % samples (68 and 141 at 20ºC and 10^3 Hz, respectively). This is related to the larger interphases formed in more doped samples (SEM images, Figure 1b) which contribute into charges accumulation. This behaviour is always present in composites, and arises from the heterogeneity in conductivity and permittivity between the filler and the matrix, giving rise to interfacial or Maxwell–Wagner–Sillars polarization [43]. However, the relative lower values of SF/ $BaTiO_3$ samples ε' when are compared with the behaviour, is ascribed to the same interphases, which have lower polarizability than the own ceramic structures. Nevertheless, the achieved ε' values are far above other $BaTiO_3$ nanocomposites with synthetic matrix [44-46].

Dielectric loss (ε″) of neat SF is between 0.1 and 10, in all the frequency range and regardless the temperature (Figure 2c). As can be observed in Figure 2d for single 40wt. % SF/$BaTiO_3$ (in function of temperature and frequency) and in Figure 2f for all the samples (in function of temperature), $BaTiO_3$ nanoparticles addition, induce a substantial rise of dielectric imaginary part (up to 3680 for 40wt. % sample at 10^{-1} Hz and 140 ºC and below 13 at T < 60 ºC). $BaTiO_3$ nanoparticles dielectric relaxation is attributed to

the reorientation of titanium ions after electric field removal. Consequently, the whole structure behaves a conformational relaxation.

Regarding to frequency effect on dielectric permittivity, it can be observed that both components (ε′, ε′′) decrease with the frequency increasing. Specially at frequencies below 10^2 Hz in where a steep drop is observed for all the samples. This decreasing is around one order of magnitude for real part and around 2 orders for the imaginary part. A constant decreasing of permittivity values with frequency increasing is observed. This frequency dependence is attributed to: i) the strong and long inter- and intramolecular interactions between the charged and polar groups of the protein [47, 48], and ii) the typical nature of Maxwell–Wagner–Sillars (MWS) polarization, generated in organic/inorganic interfaces in composites due to the difference in dielectric constants [49-51]. This effect, makes that polarizable units inside the material cannot catch up with the alternating high frequencies, resulting decreased dielectric constants. Finally, regarding to the similar dielectric permittivity shape that both SF and SF/$BaTiO_3$ nanocomposites show (note the different scale between SF sample and 40wt. % SF/$BaTiO_3$ composite) suggest the presence of similar polarizable units contributing into the permittivity. Thus, taking in account the measured frequencies and used materials, the polarizable units at medium frequencies can be ascribed to ionic contributions.

The permittivity values (ε′, ε′′) in function of temperature (Figure 2e and 2f**,** respectively) were used to reveal the relaxation processes of samples. As can be observed, a wide peak observed in both permittivity values between -40 to 60 ºC, reveals a first relaxation process. This relaxation, so-called β-relaxation or low temperature relaxation is related to a molecular dynamics increasing, ascribed to silk polymer chains and bound water molecules interaction [52]. Although samples previous desiccation before measurements, the β-relaxation is preserved due to the presence of traces of highly bonded water

molecules on the system. Some authors have signalled an additional relaxation process associated with bound water removal at temperatures around 80-100 ºC [52, 53]. But this process is more related to non-bonded water molecules and thus, is not observed in this system because the desiccation. Above 170ºC, it has been reported a high temperature relaxation so-called α-relaxation and related with the motion increasing of the SF backbone due to glass transition [29, 53, 54]. However, as is well observed in Figure 2f, in this system the transition is masked by the combination of: i) the conductivity process and electrode polarization present at low frequencies and high temperature, as also occurs in other works [52] ii) the low amount of amorphous domains (Figure S3) and iii) the last dispersion process (above 190-210 ºC), related with the structures thermal decomposition beginning.

The electrode polarization effect is due to the accumulation of charge carriers at the electrode-sample interface and may be related to the dispersion observed at high temperature (>190 ºC) in Figure 2f [49] [55].

For a detailed analysis of the relaxation mechanisms in complex materials, such as polymer composites, the electric modulus formalism, M^*, is often used. This helps to revealing additional information form the dielectric spectra, since it limits the effect of electrode polarization and transforms the process related to conductivity into a relaxation peak [56-58]. In this way the masked relaxation processes can be analysed.

The complex electric modulus M^* is defined as the reciprocal of the complex relative permittivity, ε^*:

$$M^* = \frac{1}{\varepsilon^*} = M'(\omega) + iM''(\omega) = \frac{\varepsilon'(\omega)}{\varepsilon'^2(\omega)+\varepsilon''^2(\omega)} + i\frac{\varepsilon''(\omega)}{\varepsilon'^2(\omega)+\varepsilon''^2(\omega)} \quad (1)$$

Figure 3a shows the Isochronal spectra of imaginary part of the electric modulus (M'') in all the range of temperature at 1 Hz for composites as a function of the nanoparticle

concentration (up to 40%) and particle size (40wt. % SF/$BaTiO_3$ composite with nanoparticle size of 100 and 200 nm).

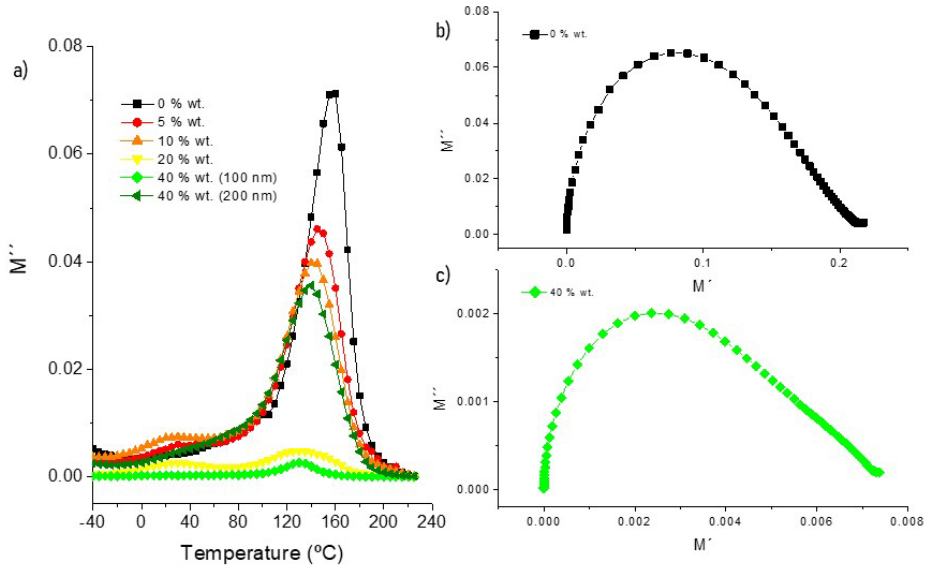

Figure 3 - a) Isochronal spectra at 1 Hz of the imaginary part of the electric modulus for the different SF/$BaTiO_3$ composites as a function of the nanoparticle concentration and size (up to 40wt. % with size 100 nm and 40wt. % with size 200 nm). Cole-Cole plot of M' vs M'' for b) SF and c) SF/ $BaTiO_3$ composite with 40wt. % of nanoparticles at 180 ºC.

In all the samples and regarding to fillers addition, two peaks can be mainly identified. These peaks can be related with relaxation processes. At low temperature (between -40 and 60ºC) a dipolar relaxation process is observed. This also identified in the isochronal diagram of ε'' depicted in Figure 2f and is associated with water molecules bound to SF chains: β-relaxation. The second process is identified at higher temperatures (between 140 and 180 ºC). This is in the range in which the imaginary part of the permittivity increases sharply (Figure 2f), and can be attributed to electric charge transport and MWS polarization, as observed in heterogeneous materials [46, 49]. As can be observed, the intensity of the peaks diminishes as $BaTiO_3$ nanoparticles content increases, signalling weaker relaxation processes because fillers high dielectric permittivity. When both

relaxation processes are compared, it is clearly noted that the related with higher temperatures (β-relaxation) is always is the main one. The ratio between both relaxations intensity is larger in samples with low fillers loading, because the relaxation is more dominated by SF matrix molecular motions, while the same effect is masked by fillers behaviour on samples with high fillers loading.

It is necessary to mention that, the 40wt. % SF/$BaTiO_3$ composite with bigger nanoparticles (200 nm) shows more intense relaxation processes than the observed for the composite with 40wt. % and 100 nm size particles. In specific, 40wt. % SF/$BaTiO_3$ with 200 nm show a close relaxation to the observed for 10wt. % SF/$BaTiO_3$ with 100 nm fillers. This signals the large influence of nanoparticles size on the SF/$BaTiO_3$ composites relaxation process and permittivity. This effect has been previously analysed by experimental, theoretical and computational studies, however there is not a real consensus about the placements of maximum permittivity values in function of $BaTiO_3$ nanoparticles size [59-61]. It is known that the dielectric property of $BaTiO_3$ particles depend on: i) impurities and defects in the crystals, ii) the volume fraction of crystalline grains composing the lattice and iii) size [59]. But additionally, it must to be considered the interactions and interphases formed between nanoparticles and matrix on composites [41, 62]. All this parameters are strongly influenced by processing conditions [46, 59, 60] and thus the permittivity values will vary between nanoparticles even with similar size. With no doubt, the present results, suggest a larger relaxation process on 200 nm samples compared with 100 nm ones.

Figures 4 shows SF/$BaTiO_3$ nanocomposites complex modulus imaginary part (M´´) as a function of all the frequency range (10^{-1} to 10^6 Hz) and temperature (between -40 ºC and 220 °C). SF and 40 wt.% SF/$BaTiO_3$ samples have been selected as representative for all the samples (Figure 4a and 4b, respectively). Once again, the two relaxation processes

are clearly observed: β-relaxation at cooler temperatures (between -40 and 40 ºC) and relaxation at high temperatures (from 140 ºC) related to conductivity. To ease the plotted data understanding, 40 and 140 ºC lines have been combined with scatters to highlight the relaxation processes ending and starting points, respectively.

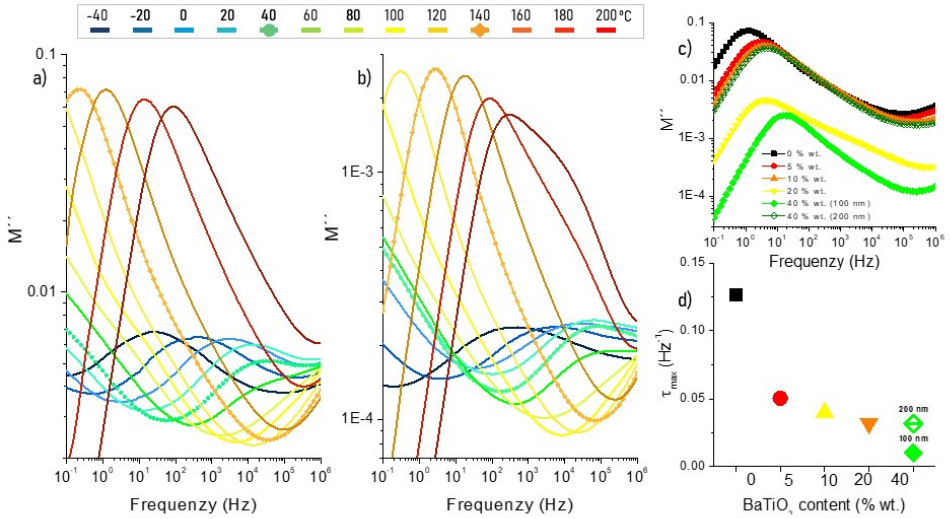

Figure 4 - Frequency dependence of the imaginary part of the electric modulus for a) SF and b) 40 wt.% SF/$BaTiO_3$ (Note the different scale in Y axis between samples). c) Comparison of electric M'' spectra of SF/$BaTiO_3$ composites at 160 ºC as a function of frequency and d) Relaxation time of SF/$BaTiO_3$ composites at 160 ºC.

As can be clearly observed, the samples relaxation is completely dependent on temperature. In all the samples, both relaxation processes maximum sift to higher frequencies as the temperature is increased. The β-relaxation is always less intense, this mainly because the larger molecular motions of SF above its glass transition (Figure S3d). In order to compare the $BaTiO_3$ addition effect, an isotherm with electric M'' spectra of all composites at 160 ºC as a function of frequency has been added (Figure 4c). At this temperature, the plotted data mainly show the relaxation dependency to fillers content. The results are in line with the obtained data at low frequencies (Figure 4a) and confirm the relaxation intensity decreasing and shifting towards higher frequencies with fillers

addition. The same data has been previously reported in other composites with $BaTiO_3$ nanoparticles [46]. As size effect comparison, the data for 40 wt.% SF/$BaTiO_3$ with 200 nm fillers has been also plotted on Figure 4c. As previously observed at low frequencies (Figure 4a), nanoparticles size increasing induce more intense relaxation processes at lower frequencies.

The frequency of the peak (v_{max}) is considered to represent a characteristic frequency or relaxation time (τ) of a given relaxation process:

$$\tau = {}^{1}/_{2\pi v_{max}} \tag{2}$$

Thus, by analysing the peaks of Figure 4c, it is possible to calculate the relaxation time τ. Results are plotted on Figure 4d. The obtained data show a relaxation time decreasing with the $BaTiO_3$ nanoparticles addition. This is in good agreement with the results reported by S. B. Aziz et. al. [63] and is ascribed to the increase of ionic mobility. In this region a transition from long-range (ionic mobility) to short-range mobility (dipolar) along conducting paths [57] is observed. Comparing the 100 nm nanoparticles with 200 nm bigger ones, it is observed that the shift to higher frequency and the peak intensity is reduced, indicating less charge mobility.

The analysis of the dynamics of the β-relaxation (cold relaxation) has been performed from the M'' spectra, where the process is more clearly observed. The parameters obtained from the electric modulus formalism can be related to those obtained from the dielectric permittivity. The relationship between the relaxation time obtained from the electric modulus and the permittivity can be expressed as:

$$\log \tau_M = \log\left(\frac{\varepsilon_\infty}{\varepsilon_s}\right) + \log \tau_\varepsilon \tag{3}$$

however, $\log\left(\frac{\varepsilon_\infty}{\varepsilon_s}\right)$ is a very small number, thus it can be considered that $\log \tau_M \approx \log \tau_\varepsilon$.

The β-relaxation time ($\tau_{\beta-relax}$) at low temperature was obtained from the maximum of the peak in the imaginary part of the electric modulus formalism. As can be observed on

Figure 5a, $\tau_{\beta-relax}$ follows the Arrhenius type temperature dependence, which is described as:

$$\tau_{\beta-relax}(T) = Ae^{\frac{E_a\,(\beta-relax)}{k_B T}} \quad (4)$$

where A is a pre-exponential factor identified as the attempt frequency, $E_{a\ (\beta\text{-}relax)}$ is the apparent activation energy of the process, T is temperature and k_B is the Boltzmann constant. For this β-relaxation and regardless of the $BaTiO_3$ concentration and particle size, the apparent activation energy (Table 1) remains almost constant. This suggest that the interactions between the silk polymer chains and bound water molecules are not significantly affected by the incorporation of nanoparticles, confirming the results obtained from FTIR data (Figure S3a-c). These values of the apparent activation energy [52 to 56 KJ/mol], are in the same range, although they are slightly higher that the value obtained from the loss tangent reported by J. Magoshi et. al. [64].

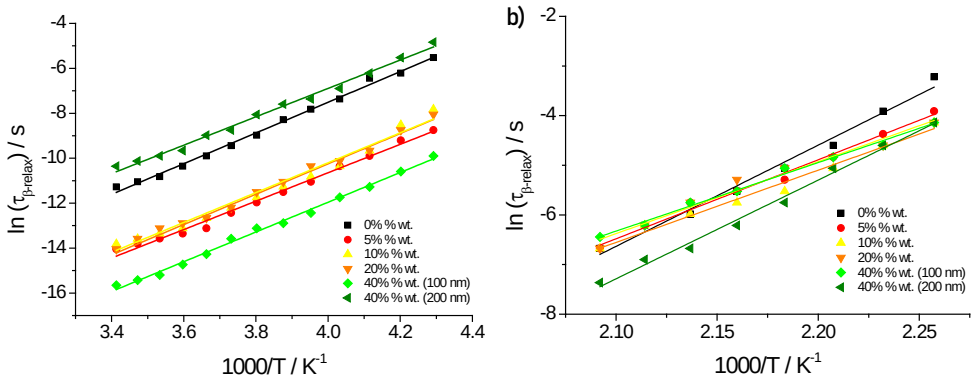

Figure 5 - Temperature dependence of the relaxation times of SF/$BaTiO_3$ composites obtained from the maximum in M″ isotherms at low- (a) and high- (b) temperature relaxation processes. Solid lines show the Arrhenius fitting.

The relaxation at higher temperature also shows an Arrhenius- behaviour, as observed in Figure 5b, indicating that the process is thermally activated. The fitting of the experimental results, obtained applying Equation 4 and identified as τ_{cond} and $E_{a\ (cond)}$, is

reported in Table 1. The apparent activation energy of the process decreases when the concentration of $BaTiO_3$ nanoparticles increases, in good agreement with previous results [46]. Large nanoparticle size produces an increase in the apparent activation energy, from around 114 KJ/mol (for nanocomposites with 40% of nanoparticles with size 100 nm) to 165 KJ/mol for size 200 nm. Smaller particles, which possess a higher ratio of surface area to volume may have better particle-to-particle contact and particle-matrix contact, improving the dielectric constant in composites [65].

Table 1 - Fitting parameters and apparent activation energy for β- and conduction relaxation of SF/$BaTiO_3$ composites obtained from the maximum of M''. At a temperature range of -40 to 20ºC.

Sample	β-relaxation		Conductivity-relaxation	
	A	$E_{a\ (\beta\text{-relax})}$ kJ·mol^{-1}	A	$E_{a\ (cond)}$ kJ·mol^{-1}
0%	7.5×10^{-16}	56.8	3.4×10^{-22}	169.5
5%	2.5×10^{-16}	52.6	4.7×10^{-18}	132.3
10%	6.6×10^{-17}	53.5	7.6×10^{-17}	121.4
20%	1.1×10^{-16}	55.3	6.9×10^{-16}	119.3
40% - 100nm	2.0×10^{-17}	55.0	4.6×10^{-16}	114.8
40% - 200nm	1.1×10^{-14}	52.5	5.1×10^{-22}	165.3

Figure S4 shows the plots of neat SF and SF/$BaTiO_3$ composites with nanoparticle concentration 10%, and 40% (size 100 nm) and 40% (size 200 nm) using normalized variables M''/M''_{max} and $\log(\omega/\omega_{max})$, with M''_{max} being the maximum value of the imaginary component of M^*, and ω_{max} the angular frequency where this maximum appears.

The shape of the curve is dependent on temperature and a master curve cannot be obtained. If the process exhibits a single relaxation time, the peak is very close and

symmetric (Debye model) [49]. However, the peak for neat SF sample, although very narrow is not totally symmetrical, deviating from the pure Debye behavior.

3.3. Conductivity formalism

To assess the effect of charge carriers and electrode polarization, the complex conductivity (σ^*) is more adequate and was calculated from the dielectric function using the following equation:

$$\sigma^* = \sigma'(\omega) + i\sigma''(\omega) = \varepsilon_0\omega\varepsilon''(\omega) + i\varepsilon_0\omega\varepsilon'(\omega) \qquad (5)$$

where ε_0 ($8.85\text{x}10^{-12}$ Fm^{-1}) is the permittivity of free space and $\omega = 2\pi\nu$ is the angular frequency.

Figure 6 shows the real part of the complex conductivity, σ*(ω), for SF/$BaTiO_3$ composites with 0wt.%, 10 wt.%, 40 wt.% (size100 nm) and 40 wt.% (size 200 nm). For the remaining composites, the conductivity formalism reveals similar results.

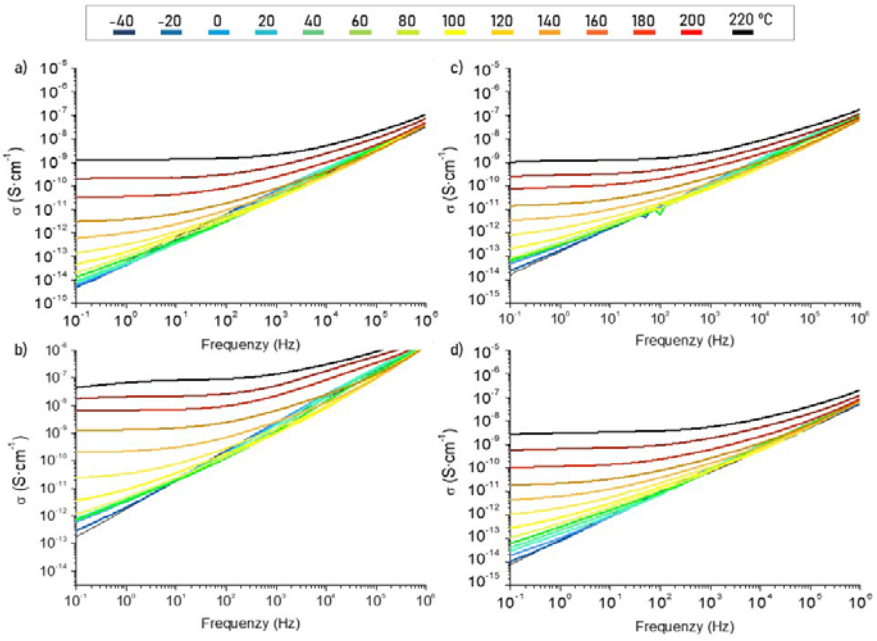

Figure 6 - Frequency dependence of the real part of the conductivity (σ') at different temperatures for SF/$BaTiO_3$ composites with a) 0wt.%, b) 10 wt.%, c), 40 wt.% (100 nm) d) and 40 wt.% (200 nm).

Regardless $BaTiO_3$ concentration, particle size, and temperature, it can be observed that the real part of the conductivity, σ', increases with increasing frequency (Figure 6). All SF/$BaTiO_3$ samples show a plateau at low frequency range that can be ascribed as the *dc*-conductivity, being broader as temperature increases. In this region, the conductivity is frequency independent and is equal to the bulk conductivity of the sample. In addition, in the σ' spectrum of SF/$BaTiO_3$ composites, it is observed a decrease of the conductivity at low frequencies and high temperature isotherms, which is related to electrode polarization. This effect is particularly noticeable in the composite with 40 wt.% of $BaTiO_3$ nanoparticles with size 100 nm (Figure 6c).

From low to high frequencies, the σ' plot presents an initial increase due to the blocking effect of the charge carriers [66], the plateau related to *dc*-conductivity (σ_0), where the conductivity is independent of the frequency and the linear increase of the electrical conductivity with frequency, i.e. ac-conductivity. In the transition region from *dc*- A.C conductivity, the charge carriers change from long-range to short-range mobility along conducting paths [57].

Figure 7 shows the *dc*-conductivity (σ_0) vs the inverse temperature, at T ≥ 170 ºC, which yields a straight line. The activation energy, $E_{a\ (dc\text{-}cond)}$, can be calculated using the Arrhenius equation:

$$\sigma_o(T) = Be^{\frac{E_{a\,(dc-cond)}}{k_B T}} \quad (6)$$

where *B* is a pre-exponential factor identified as the attempt frequency, $E_{a\ (dc\text{-}cond)}$ is the apparent activation energy of the process, T is temperature and k_B is the Boltzmann constant. The results are indicated in Table 2.

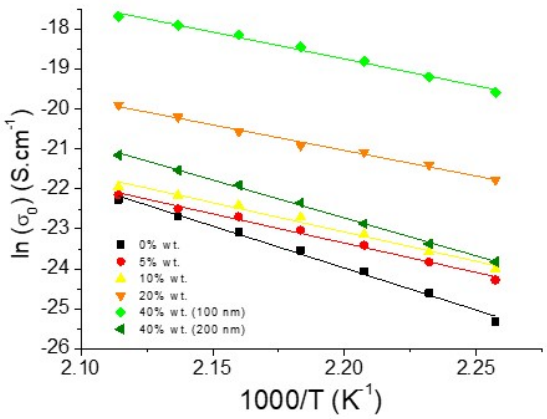

Figure 7 - *dc*-conductivity as a function of temperature for all SF/$BaTiO_3$ composites from 170 to 200 ºC. Solid lines show Arrhenius fitting.

Table 2 - Fitting parameter and activation energy for the dc-conductivity for all SF/$BaTiO_3$ composites in the temperature range between 170 and 200 ºC

Sample	**A**	**E_a (dc-cond) / kJ.mol^{-1}**
0%	4.7×10^{9}	174.8
5%	2.1×10^{5}	134.4
10%	9.6×10^{3}	130.2
20%	1.2×10^{3}	106.3
40% - 100nm	4.8×10^{4}	112.2
40% - 200nm	1.9×10^{8}	157.9

The highest activation energy is found for the SF sample. The composites show a strong decrease in comparison to neat SF, being the differences for the increase in nanoparticles concentration (and size) much smaller compared to the strong reduction with respect to the polymer matrix. The activation energy for the composite with larger nanoparticle size (200 nm, concentration 40%) is higher than that obtained in the composite with smaller size (100 nm, concentration 40%), suggesting that the number of dipoles formed on the interface between the ceramic particles and the matrix is lower due to reduction in the surface/volume ratio in the nanoparticles with larger size.

The activation energies calculated for the *dc*-conductivity are quite close to those calculated from the peak at high temperature in (Figure 4c and Table 1). It has been

reported that both the ionic conductivity and the dc-conductivity possess the same temperature-dependence [52], thus the position (frequency) of the peak in *M''* spectrum represents the conductivity relaxation.

4. Conclusion

Silk fibroin (SF) nanocomposites with $BaTiO_3$ have been developed with varying filler concentration (up to 40%) and size (100 and 200 nm) in order to tailor the dielectric response. The composites have been investigated by means of morphological and broad band dielectric spectroscopy. Filler concentration and size does not affect the morphology of the SF, thus it has been possible to obtain for all the cases self-standing films with high optical transparency levels. Due to variable Fillers concentrations, it is possible to control the samples dielectric constant from 4.4 in SF to 142 in the SF/$BaTiO_3$ composite with 40wt.% (20 ºC, 1 kHz), the dielectric constant depending on both $BaTiO_3$ concentration and particle size. Through the electric modulus M*(ω) formalism, it has been analyzed the low-temperature β-relaxation, related to the interaction between the silk polymer chains and bound water molecules, and the conductivity relaxation that takes place at higher temperatures. The β-relaxation peak shift slightly to lower temperature in SF/$BaTiO_3$ composites compared to the SF sample and its process intensity decreases when the nanoparticle content (with a size of 100 nm) increases. The MWS process was observed in the composites, related to the interface areas between the nanoparticles and the SF matrix. For all SF/$BaTiO_3$ composites, *dc*-conductivity increases with temperature and the apparent activation energy of the process decreases with increasing $BaTiO_3$ concentration and the incorporation of nanoparticles with smaller size. Thus, this works demonstrate that natural based materials can be tuned in terms of their dielectric properties in order to play a relevant role in the next generation of sustainable electronic devices.

Acknowledgements

The authors thank the FCT (Fundação para a Ciência e Tecnologia) for financial support under the framework of Strategic Funding grants UID/FIS/04650/2019, and UID/EEA/04436/2019; and project PTDC/FIS-MAC/28157/2017. The author also thanks the FCT for financial support under grant SFRH/BPD/112547/2015 and Investigator FCT Contract 2020.04028.CEECIND (C.M.C.) as well POCH and European Union. Financial support from the Spanish Ministry of Science and Innovation (MCINN, Agencia Estatal de Investigación) through the project RTI2018-097862-B-C21 and MAT2016-76039-C4-3-R (AEI/FEDER, UE) (including the FEDER financial support) and from the Basque Government Industry and Education Departments under the ELKARTEK, HAZITEK and PIBA (PIBA-2018-06) programs, respectively, are acknowledged. CIBER-BBN is an initiative funded by the VI National R&D&I Plan 2008–2011, Iniciativa Ingenio 2010, Consolider Program. CIBER Actions are financed by the Instituto de Salud Carlos III with assistance from the European Regional Development Fund.

References

[1] Law KL. Plastics in the Marine Environment. Annual Review of Marine Science. 2017;9(1):205-29.
[2] Mercado G, Dominguez M, Herrera I, Melgoza R. Are Polymers Toxic? Case Study: Environmental Impact of a Biopolymer. J Environ Sci Eng B. 2017;6:121-6.
[3] Murray A, Skene K, Haynes K. The Circular Economy: An Interdisciplinary Exploration of the Concept and Application in a Global Context. Journal of Business Ethics. 2017;140(3):369-80.
[4] Jawahir IS, Bradley R. Technological Elements of Circular Economy and the Principles of 6R-Based Closed-loop Material Flow in Sustainable Manufacturing. Procedia CIRP. 2016;40:103-8.
[5] Zhijun F, Nailing Y. Putting a circular economy into practice in China. Sustainability Science. 2007;2(1):95-101.
[6] Payne J, McKeown P, Jones MD. A circular economy approach to plastic waste. Polymer Degradation and Stability. 2019;165:170-81.
[7] Hildebrandt J, Bezama A, Thrän D. Cascade use indicators for selected biopolymers: Are we aiming for the right solutions in the design for recycling of bio-based polymers? Waste Management & Research. 2017;35(4):367-78.
[8] Reizabal A, Costa CM, Saiz PG, Gonzalez B, Pérez-Álvarez L, Fernández de Luis R, et al. Processing Strategies to Obtain Highly Porous Silk Fibroin Structures with Tailored Microstructure and Molecular Characteristics and Their Applicability in Water Remediation. Journal of Hazardous Materials. 2021;403:123675.

[9] Asakura T, Okushita K, Williamson MP. Analysis of the Structure of Bombyx mori Silk Fibroin by NMR. Macromolecules. 2015;48(8):2345-57.
[10] Zhou C-Z, Confalonieri F, Medina N, Zivanovic Y, Esnault C, Yang T, et al. Fine organization of Bombyx mori fibroin heavy chain gene. Nucleic Acids Research. 2000;28(12):2413-9.
[11] Zhou C-Z, Confalonieri F, Jacquet M, Perasso R, Li Z-G, Janin J. Silk fibroin: Structural implications of a remarkable amino acid sequence. Proteins: Structure, Function, and Bioinformatics. 2001;44(2):119-22.
[12] Sommer MR, Schaffner M, Carnelli D, Studart AR. 3D Printing of Hierarchical Silk Fibroin Structures. ACS Applied Materials & Interfaces. 2016;8(50):34677-85.
[13] Shen T, Wang T, Cheng G, Huang L, Chen L, Wu D. Dissolution behavior of silk fibroin in a low concentration CaCl2-methanol solvent: From morphology to nanostructure. International Journal of Biological Macromolecules. 2018;113:458-63.
[14] Reizabal A, Gonçalves S, Brito-Pereira R, Costa P, Costa CM, Pérez-Álvarez L, et al. Optimized silk fibroin piezoresistive nanocomposites for pressure sensing applications based on natural polymers. Nanoscale Advances. 2019;1(6):2284-92.
[15] Reizabal A, Brito-Pereira R, Fernandes MM, Castro N, Correia V, Ribeiro C, et al. Silk fibroin magnetoactive nanocomposite films and membranes for dynamic bone tissue engineering strategies. Materialia. 2020;12:100709.
[16] Rockwood DN, Preda RC, Yücel T, Wang X, Lovett ML, Kaplan DL. Materials fabrication from Bombyx mori silk fibroin. Nature Protocols. 2011;6(10):1612-31.
[17] Murugesh Babu K. 13 - Silk from silkworms and spiders as high-performance fibers. In: Bhat G, editor. Structure and Properties of High-Performance Fibers. Oxford: Woodhead Publishing; 2017. p. 327-66.
[18] Zhang L, Liu X, Li G, Wang P, Yang Y. Tailoring degradation rates of silk fibroin scaffolds for tissue engineering. Journal of Biomedical Materials Research Part A. 2019;107(1):104-13.
[19] Tungtasana H, Shuangshoti S, Shuangshoti S, Kanokpanont S, Kaplan DL, Bunaprasert T, et al. Tissue response and biodegradation of composite scaffolds prepared from Thai silk fibroin, gelatin and hydroxyapatite. Journal of Materials Science: Materials in Medicine. 2010;21(12):3151-62.
[20] Noishiki Y, Nishiyama Y, Wada M, Kuga S, Magoshi J. Mechanical properties of silk fibroin–microcrystalline cellulose composite films. Journal of Applied Polymer Science. 2002;86(13):3425-9.
[21] Cai Z-x, Mo X-m, Zhang K-h, Fan L-p, Yin A-l, He C-l, et al. Fabrication of Chitosan/Silk Fibroin Composite Nanofibers for Wound-dressing Applications. International Journal of Molecular Sciences. 2010;11(9):3529-39.
[22] Reizabal A, Correia DM, Costa CM, Perez-Alvarez L, Vilas-Vilela JL, Lanceros-Méndez S. Silk Fibroin Bending Actuators as an Approach Toward Natural Polymer Based Active Materials. ACS Applied Materials & Interfaces. 2019;11(33):30197-206.
[23] Gao A, Xie K, Song X, Zhang K, Hou A. Removal of the heavy metal ions from aqueous solution using modified natural biomaterial membrane based on silk fibroin. Ecological Engineering. 2017;99:343-8.
[24] Baek DH, Ki CS, Um IC, Park YH. Metal ion adsorbability of electrospun wool keratose/silk fibroin blend nanofiber mats. Fibers and Polymers. 2007;8(3):271-7.
[25] Kundu J, Chung Y-I, Kim YH, Tae G, Kundu SC. Silk fibroin nanoparticles for cellular uptake and control release. International Journal of Pharmaceutics. 2010;388(1):242-50.
[26] Koh L-D, Yeo J, Lee YY, Ong Q, Han M, Tee BCK. Advancing the frontiers of silk fibroin protein-based materials for futuristic electronics and clinical wound-healing (Invited review). Materials Science and Engineering: C. 2018;86:151-72.
[27] Zhu B, Wang H, Leow WR, Cai Y, Loh XJ, Han M-Y, et al. Silk Fibroin for Flexible Electronic Devices. Advanced Materials. 2016;28(22):4250-65.
[28] Qin X, Peng Y, Li P, Cheng K, Wei Z, Liu P, et al. Silk fibroin and ultra-long silver nanowire based transparent, flexible and conductive composite film and its Temperature-Dependent resistance. International Journal of Optomechatronics. 2019;13(1):41-50.

[29] Reizabal A, Gonçalves S, Pereira N, Costa CM, Pérez L, Vilas-Vilela JL, et al. Optically transparent silk fibroin/silver nanowire composites for piezoresistive sensing and object recognitions. Journal of Materials Chemistry C. 2020;8(37):13053-62.
[30] Lee M, Jeon H, Kim S. A Highly Tunable and Fully Biocompatible Silk Nanoplasmonic Optical Sensor. Nano Letters. 2015;15(5):3358-63.
[31] Kujala S, Mannila A, Karvonen L, Kieu K, Sun Z. Natural Silk as a Photonics Component: a Study on Its Light Guiding and Nonlinear Optical Properties. Scientific Reports. 2016;6(1):22358.
[32] Shi L, Xu X, Ma M, Li L. High-performance, low-operating voltage, and solution-processable organic field-effect transistor with silk fibroin as the gate dielectric. Applied Physics Letters. 2014;104(2):023302.
[33] Wang C-H, Hsieh C-Y, Hwang J-C. Flexible Organic Thin-Film Transistors with Silk Fibroin as the Gate Dielectric. Advanced Materials. 2011;23(14):1630-4.
[34] Kim KN, Chun J, Chae SA, Ahn CW, Kim IW, Kim S-W, et al. Silk fibroin-based biodegradable piezoelectric composite nanogenerators using lead-free ferroelectric nanoparticles. Nano Energy. 2015;14:87-94.
[35] Park K-I, Lee M, Liu Y, Moon S, Hwang G-T, Zhu G, et al. Flexible Nanocomposite Generator Made of BaTiO3 Nanoparticles and Graphitic Carbons. Advanced Materials. 2012;24(22):2999-3004.
[36] Sencadas V, Garvey C, Mudie S, Kirkensgaard JJK, Gouadec G, Hauser S. Electroactive properties of electrospun silk fibroin for energy harvesting applications. Nano Energy. 2019;66:104106.
[37] Jacob J, More N, Mounika C, Gondaliya P, Kalia K, Kapusetti G. Smart Piezoelectric Nanohybrid of Poly(3-hydroxybutyrate-co-3-hydroxyvalerate) and Barium Titanate for Stimulated Cartilage Regeneration. ACS Applied Bio Materials. 2019;2(11):4922-31.
[38] Luo C, Hu S, Xia M, Li P, Hu J, Li G, et al. A Flexible Lead-Free BaTiO3/PDMS/C Composite Nanogenerator as a Piezoelectric Energy Harvester. Energy Technology. 2018;6(5):922-7.
[39] Williams G, Begum S. Polymers, Dielectric Properties of. Reference Module in Materials Science and Materials Engineering: Elsevier; 2017.
[40] Pitera JW, Falta M, van Gunsteren WF. Dielectric Properties of Proteins from Simulation: The Effects of Solvent, Ligands, pH, and Temperature. Biophysical Journal. 2001;80(6):2546-55.
[41] Mendes-Felipe C, Rodrigues-Marinho T, Vilas JL, Lanceros-Mendez S. UV curable nanocomposites with tailored dielectric response. Polymer. 2020;196:122498.
[42] Wang Y, Liu YB, Hu XH, He YT, Gao JH, Zhong LS. High dielectric permittivity in BaTiO3−xBaSnO3 ceramics. 2017 1st International Conference on Electrical Materials and Power Equipment (ICEMPE)2017. p. 507-10.
[43] Sun H, Zhang H, Liu S, Ning N, Zhang L, Tian M, et al. Interfacial polarization and dielectric properties of aligned carbon nanotubes/polymer composites: The role of molecular polarity. Composites Science and Technology. 2018;154:145-53.
[44] Phan TTM, Chu NC, Luu VB, Nguyen Xuan H, Martin I, Carriere P. The role of epoxy matrix occlusions within BaTiO3 nanoparticles on the dielectric properties of functionalized BaTiO3/epoxy nanocomposites. Composites Part A: Applied Science and Manufacturing. 2016;90:528-35.
[45] Emelianov NA, Postnikov EB, Yacovlev OV, Chaplygin AA, Chekadanov AS, Al Mandalavi WM. Dielectric relaxation and charge transfer mechanism in the composite material of nanoparticles BaTiO3 with a modified surface in polystyrene. The European Physical Journal B. 2015;88(11):291.
[46] Chanmal C. Dielectric relaxations in PVDF/BaTiO3 nanocomposites. Express Polymer Letters - EXPRESS POLYM LETT. 2008;2:294-301.
[47] Simonson T. Dielectric relaxation in proteins: the computational perspective. Photosynthesis Research. 2008;97(1):21.
[48] Bibi F, Villain M, Guillaume C, Sorli B, Gontard N. A Review: Origins of the Dielectric Properties of Proteins and Potential Development as Bio-Sensors. Sensors. 2016;16(8):1232.

[49] Kremer F, Schönhals A. Broadband Dielectric Spectroscopy: Springer Berlin Heidelberg; 2002.
[50] Pan Z, Yao L, Zhai J, Shen B, Wang H. Significantly improved dielectric properties and energy density of polymer nanocomposites via small loaded of BaTiO3 nanotubes. Composites Science and Technology. 2017;147:30-8.
[51] Jian G, Jiao Y, Meng Q, Wei Z, Zhang J, Yan C, et al. Enhanced dielectric constant and energy density in a BaTiO3/polymer-matrix composite sponge. Communications Materials. 2020;1(1):91.
[52] Yu L, Hu X, Kaplan D, Cebe P. Dielectric Relaxation Spectroscopy of Hydrated and Dehydrated Silk Fibroin Cast from Aqueous Solution. Biomacromolecules. 2010;11(10):2766-75.
[53] Um IC, Kim TH, Kweon HY, Ki CS, Park YH. A comparative study on the dielectric and dynamic mechanical relaxation behavior of the regenerated silk fibroin films. Macromolecular Research. 2009;17(10):785-90.
[54] Hu X, Kaplan D, Cebe P. Dynamic Protein−Water Relationships during β-Sheet Formation. Macromolecules. 2008;41(11):3939-48.
[55] Frenzel F, Guterman R, Anton AM, Yuan J, Kremer F. Molecular Dynamics and Charge Transport in Highly Conductive Polymeric Ionic Liquids. Macromolecules. 2017;50(10):4022-9.
[56] Correia DM, Costa CM, Sabater i Serra R, Gómez Tejedor JA, Teruel Biosca L, de Zea Bermudez V, et al. Molecular relaxation and ionic conductivity of ionic liquids confined in a poly(vinylidene fluoride) polymer matrix: Influence of anion and cation type. Polymer. 2019;171:58-69.
[57] Xu P, Zhang X. Investigation of MWS polarization and dc conductivity in polyamide 610 using dielectric relaxation spectroscopy. European Polymer Journal. 2011;47(5):1031-8.
[58] Sabater i Serra R, Molina-Mateo J, Torregrosa-Cabanilles C, Andrio-Balado A, Meseguer Dueñas JM, Serrano-Aroca Á. Bio-Nanocomposite Hydrogel Based on Zinc Alginate/Graphene Oxide: Morphology, Structural Conformation, Thermal Behavior/Degradation, and Dielectric Properties. Polymers. 2020;12(3):702.
[59] Hoshina T, Wada S, Kuroiwa Y, Tsurumi T. Composite structure and size effect of barium titanate nanoparticles. Applied Physics Letters. 2008;93(19):192914.
[60] Lin S, Lü T, Jin C, Wang X. Size effect on the dielectric properties of ${\mathrm{BaTiO}}_{3}$ nanoceramics in a modified Ginsburg-Landau-Devonshire thermodynamic theory. Physical Review B. 2006;74(13):134115.
[61] Curecheriu L, Buscaglia MT, Buscaglia V, Zhao Z, Mitoseriu L. Grain size effect on the nonlinear dielectric properties of barium titanate ceramics. Applied Physics Letters. 2010;97(24):242909.
[62] Feng Y, Li J-L, Li W-L, Li M-L, Chi Q-G, Zhang T-D, et al. Effect of BaTiO3 nanowire distribution on the dielectric and energy storage performance of double-layer PVDF-based composites. Composites Part A: Applied Science and Manufacturing. 2019;125:105524.
[63] B. Aziz S, Karim W, Qadir K, Zafar Q. Proton Ion Conducting Solid Polymer Electrolytes Based on Chitosan Incorporated with Various Amounts of Barium Titanate (BaTiO3). International journal of electrochemical science. 2018;13.
[64] Magoshi J, Magoshi Y. Physical properties and structure of silk. II. Dynamic mechanical and dielectric properties of silk fibroin. Journal of Polymer Science: Polymer Physics Edition. 1975;13(7):1347-51.
[65] Yoon J-R, Han J-W, Lee K-M. Dielectric Properties of Polymer-ceramic Composites for Embedded Capacitors. Transactions on Electrical and Electronic Materials. 2009;10(4):116-20.
[66] Wang P, Xu P, Wei H, Fang H, Ding Y. Effect of block copolymer containing ionic liquid moiety on interfacial polarization in PLA/PCL blends. Journal of Applied Polymer Science. 2018;135(16):46161.